Metal–insulator-transition engineering by modulation tilt-control in perovskite nickelates for room temperature optical switching

Zhaoliang Liao[a,1,2], Nicolas Gauquelin[b,1], Robert J. Green[c,d,e,1], Knut Müller-Caspary[b], Ivan Lobato[b], Lin Li[a], Sandra Van Aert[b], Johan Verbeeck[b], Mark Huijben[a], Mathieu N. Grisolia[f], Victor Rouco[f], Ralph El Hage[f], Javier E. Villegas[f], Alain Mercy[g], Manuel Bibes[f], Philippe Ghosez[g], George A. Sawatzky[c,d], Guus Rijnders[a], and Gertjan Koster[a,2]

[a]MESA$^+$ Institute for Nanotechnology, University of Twente, 7500 AE Enschede, The Netherlands; [b]Electron Microscopy for Materials Science (EMAT), University of Antwerp, 2020 Antwerp, Belgium; [c]Quantum Matter Institute, University of British Columbia, Vancouver, V6T 1Z4, Canada; [d]Department of Physics and Astronomy, University of British Columbia, Vancouver, V6T 1Z4, Canada; [e]Department of Physics and Engineering Physics, University of Saskatchewan, Saskatoon, S7N 5E2, Canada; [f]Unité Mixte de Physique CNRS/Thales, Université Paris-Saclay, 91767 Palaiseau, France; and [g]Theoretical Materials Physics, Quantum Materials Center (Q-MAT), Complex and Entangled Systems from Atoms to Materials (CESAM), Université de Liège, B-4000 Liège, Belgium

Edited by Zachary Fisk, University of California, Irvine, CA, and approved August 8, 2018 (received for review April 30, 2018)

In transition metal perovskites ABO_3, the physical properties are largely driven by the rotations of the BO_6 octahedra, which can be tuned in thin films through strain and dimensionality control. However, both approaches have fundamental and practical limitations due to discrete and indirect variations in bond angles, bond lengths, and film symmetry by using commercially available substrates. Here, we introduce modulation tilt control as an approach to tune the ground state of perovskite oxide thin films by acting explicitly on the oxygen octahedra rotation modes—that is, directly on the bond angles. By intercalating the prototype $SmNiO_3$ target material with a tilt-control layer, we cause the system to change the natural amplitude of a given rotation mode without affecting the interactions. In contrast to strain and dimensionality engineering, our method enables a continuous fine-tuning of the materials' properties. This is achieved through two independent adjustable parameters: the nature of the tilt-control material (through its symmetry, elastic constants, and oxygen rotation angles), and the relative thicknesses of the target and tilt-control materials. As a result, a magnetic and electronic phase diagram can be obtained, normally only accessible by A-site element substitution, within the single $SmNiO_3$ compound. With this unique approach, we successfully adjusted the metal–insulator transition (MIT) to room temperature to fulfill the desired conditions for optical switching applications.

transition metal oxide | structural modulation | metal–insulator transition | heterostructure | octahedral rotation

Oxide heterostructures offer unprecedented opportunities to manipulate the interplay between spin, charge, orbital, and lattice degrees of freedom, leading to many novel electronic phases that are hard or even impossible to be realized in bulk materials (1–7). To date, strain and dimensionality are two main approaches used to engineer properties of heterostructures (in oxides ranging from dielectric or ferroelectric insulators to superconductors). While both can strongly modify the physical response of the materials (1–5), they suffer several limitations, in particular in the context of oxide perovskites whose physical properties are largely driven by the metal–oxygen bond angles (8–10). First, the strain and dimensionality engineering are both discrete handles with restricted tuning possibilities. The strain is applied through the growth on a handful of commercial substrates that have preset lattice constants, and the small lattice mismatch that is required for coherent epitaxial growth further limits the choice of substrates. Dimensionality is tuned by reducing the number of unit cells one-by-one, and a significant effect only occurs when the thickness is in the range of a few unit cells. Second, the strain often acts in an indirect manner: It will influence the bond angles but also the bond lengths, which can result in nonsystematic behavior.

The nickelates have been attracting enormous attention owing to their intriguing properties (4, 7, 10–15). One of the remarkable properties is the metal–insulator transition (MIT), which in the bulk can be continuously adjusted by tolerance factor or external pressure (10, 16), serving as a fascinating platform for both fundamental physics investigation and synaptic applications (11–19). Very recently, Mercy et al. (19) identified that the breathing mode responsible for the MIT in the perovskite nickelates is triggered by octahedral rotations and tilts. This makes the nickelates an ideal system for exploring emergent functionalities through the direct control of angles between neighboring octahedra.

In this work, we introduce modulation tilt control as an approach to tune the ground state of nickelate thin films by directly acting on the oxygen octahedral rotation modes. Through intercalating the target material with a tilt-control layer (TCL) as shown by the sketch in Fig. 1, the natural amplitude of a given rotation mode will

Significance

Correlated transition metal oxide perovskites receive a lot of attention due to their unique physical properties, which are largely driven by distortion of the BO_6 octahedral network. In bulk, the control of the octahedral network is normally obtained by cation substitutions in a random alloy. Similar to the charge donors in semiconductors, cation substitutions will introduce scattering and disorder. The development of artificial heterostructures offers unprecedented opportunities to lattice engineering to achieve desired properties. In this work, we demonstrated a structural analogue of modulation doping in nickelate heterostructures through the interfacial transfer of tilt patterns. Modulation tilt control was used to remotely control the Ni–O bonds in the compound $SmNiO_3$ and thereby its critical temperature for optimal optical switching application.

Author contributions: Z.L. contributed concept design, film growth, and transport measurements; Z.L., R.J.G, M.H., G.R., and G.K. analyzed data; Z.L. and L.L. performed atomic force microscopy and X-ray diffraction; N.G. and J.V. took STEM measurements; N.G., K.M.-C., I.L., and S.V.A. performed STEM image analysis; R.J.G. and G.A.S. took X-ray absorption spectroscopy measurements; M.N.G., V.R., R.E.H., J.E.V., and M.B. took optical measurements; A.M. and P.G. contributed Landau modelling; Z.L., N.G., R.J.G, K.M.-C., I.L., L.L., S.V.A., J.V., M.H., M.N.G., V.R., R.E.H., J.E.V., A.M., M.B., P.G., G.A.S., G.R., and G.K. extensively discussed the results; and Z.L., N.G., R.J.G, K.M.-C., I.L., L.L., S.V.A., J.V., M.H., M.N.G., V.R., R.E.H., J.E.V., A.M., M.B., P.G., G.A.S., G.R., and G.K. wrote the paper.

The authors declare no conflict of interest.

This article is a PNAS Direct Submission.

[1]Z.L., N.G., and R.J.G. contributed equally to this work.

[2]To whom correspondence may be addressed. Email: z.liao@utwente.nl or g.koster@utwente.nl.

This article contains supporting information online at www.pnas.org/lookup/suppl/doi:10.1073/pnas.1807457115/-/DCSupplemental.

Published online September 5, 2018.

be modified to retain the connectivity of the octahedral network (20, 21), leading to strong propagation of the tilt around the in-plane axes. As also shown in Fig. 1*A*, a less tilted TCL can significantly reduce the tilt in the target material. If the tilt of TCL is similar to the target material, the structure modulation effect then will be very small (Fig. 1*B*). Additionally, the decay nature of tilt propagation should allow us to modulate the tilt by changing the thickness of the target material. In contrast with strain and dimensionality engineering, our method enables a pseudocontinuous fine-tuning of the materials' properties. This is achieved through two independent adjustable parameters: the nature of the tilt-control material (through its symmetry, elastic constants, and oxygen rotation angles), and the relative thicknesses of the target and tilt-control materials. In a prototypical system where we combine $SmNiO_3$ (SNO) with TCLs in fine period TCL/SNO superlattices (SLs), we are able to directly act on the SNO octahedral rotation mode and therefore continuously tune the MIT. Our results show that a magnetic and electronic nickelate phase diagram, normally built through A-site element substitution, can be demonstrated in a single SNO compound through the transfer of tilt patterns. This remote control of ground state properties, not through doping but here through the transfer of tilt patterns, can be viewed as a structural analog of modulation doping in semiconductors. This approach paves a way for novel phases in oxides that remain inaccessible by simple composition modulations. Moreover, it offers a method to adjust materials to meet practical conditions for applications.

Results

Nickelate SLs were grown on atomically flat $NdGaO_3$ (NGO) (110) substrates by pulsed laser deposition (PLD) (*SI Appendix*, section 1). $LaFeO_3$ (LFO) was chosen as the TCL layer because LFO is less tilted than SNO, and it also shares same polar nature and orthorhombic symmetry as SNO. Additionally, a large compressive strain (1.8%) enforced by the NGO substrate will further reduce the tilt of LFO (22, 23). Therefore, a strong tilt modulation of SNO by LFO can be expected. Four unit cells (uc) of LFO were deposited first, and subsequently, the $(LFO_1/SNO_n)_m$ SLs (noted as LFO_1–SNO_n) were grown starting from SNO. The total SNO thickness ($n \times m$) was maintained at ~40 uc. The SNO films and LFO_1–SNO_n SLs share the same orthorhombic symmetry as characterized by X-ray diffraction (*SI Appendix*, section 2). Due to the presence of LFO, the LFO_1–SNO_n SLs are found to exhibit less structural distortion compared with pure SNO films.

The layer-resolved lattice distortion of nickelate SLs was investigated by scanning transmission electron microscopy (STEM). The orthorhombic symmetry produces out-of-phase tilts of amplitude (α_T) and in-phase rotations of amplitude (α_R) around the in-plane [1-10] and [001] axis, respectively. These rotational behaviors are revealed microscopically by resolving the oxygen sites in the annular bright field (ABF) images (Fig. 2 *A* and *B*). The limited contrast difference between LFO and SNO in STEM images is due to the similarity in atomic number for Sm and La, as well as Ni and Fe, but the chemical contrast can be resolved by electron energy loss spectroscopy (EELS) (*SI Appendix*, sections 3 and 4). The ABF image of the (1–10) plane displays significantly elongated and blurred oxygen sites, which are consistent with the signature of out-of-phase rotation that generates two very close oxygen columns (O_1 and O_2) (Fig. 2*A*). In the (001) plane, the atomically resolved oxygen sites clearly confirm the in-phase rotational behavior around the [001] axis (Fig. 2*B*).

Using statistical parameter estimation theory to quantify the atomic positions from a STEM image, we are able to obtain detailed, layer-resolved lattice structure parameters across the SLs (*SI Appendix*, section 5). Fig. 2*C* shows an example of the 2D mapping of the anti-polar A motion of LFO_1–SNO_{10} SL, which is described by angle (Φ) (see definition in Fig. 2*A*). The angle Φ is correlated with amplitudes of rotations (α_R) and tilts (α_T) of the BO_6 octahedra: $\Phi \sim \alpha_R \cdot \alpha_T$ (24, 25). The layer-resolved profile of Φ in LFO_1–SNO_{10} is shown in Fig. 2*D*. To avoid possible artifacts from the imaging technique itself, the profiles are normalized to the value of the NGO substrate ($\Phi_N = \Phi/\Phi_{NGO}$). As shown in Fig. 2*D*, a relaxation of the angle Φ_N is observed within the central part of the first 4-uc LFO layer, while near both the bottom LFO/NGO and top SNO/LFO interfaces, this angle Φ_N is larger, as expected from the geometric constraint effect

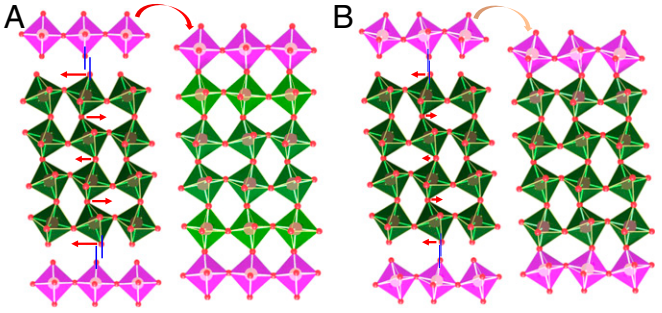

Fig. 1. Octahedral tilt pattern modulation. Schematic view of octahedral tilt modulation (green layer) by introducing a tilt-control layer (purple layer) having (*A*) less tilting and (*B*) more tilting. Here, an orthorhombic structure ($a^+b^-b^-$) is used for demonstration. The red arrows and their lengths indicate the direction and amount of the rotation angle change, respectively, which are necessary to match TCL. A smaller tilt change in interior layers is due to the decay nature of interfacial geometry constraint.

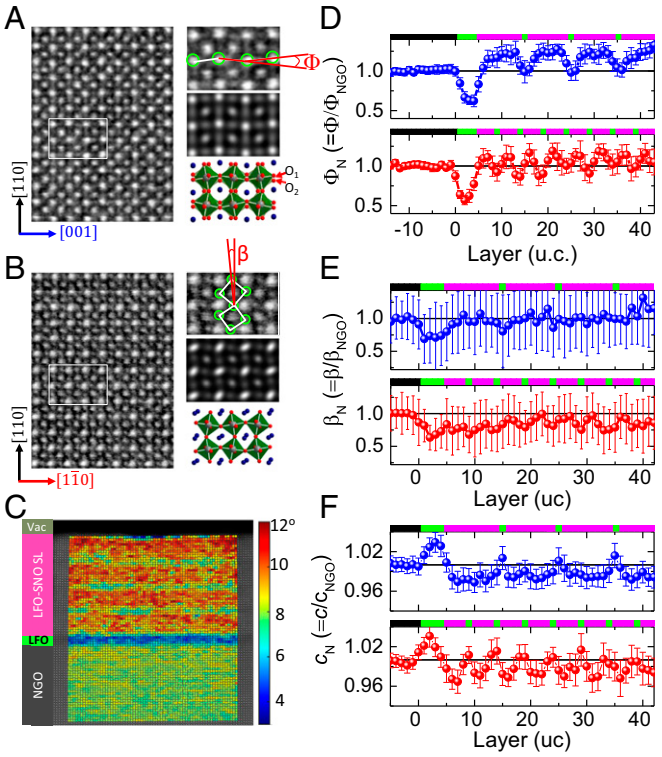

Fig. 2. Atomic scale lattice structural characterization. Inversed ABF images of LFO_1–SNO_4 with zone axis along (*A*) [1-10] and (*B*) [001] directions. (*A* and *B*, *Right*) Magnifications of a selected region (*Top*), simulated ABF-STEM images (*Middle*), and structural models of bulk SNO (*Bottom*) for comparison. (*C*) 2D mapping of antipolar A-site motions (Φ) in LFO_1–SNO_{10}. The Φ mapping is overlaid on a HAADF image from which the angle Φ is calculated. The profile of (*D*) antipolar motion (Φ), (*E*) octahedral tilt (β), and (*F*) out-of-plane lattice parameter *c* for LFO_1–SNO_4 (red) and LFO_1–SNO_{10} (blue). (*D*–*F*, *Top*) The corresponding schematic view of chemical profiles with black (NGO), green (LFO), and purple (SNO).

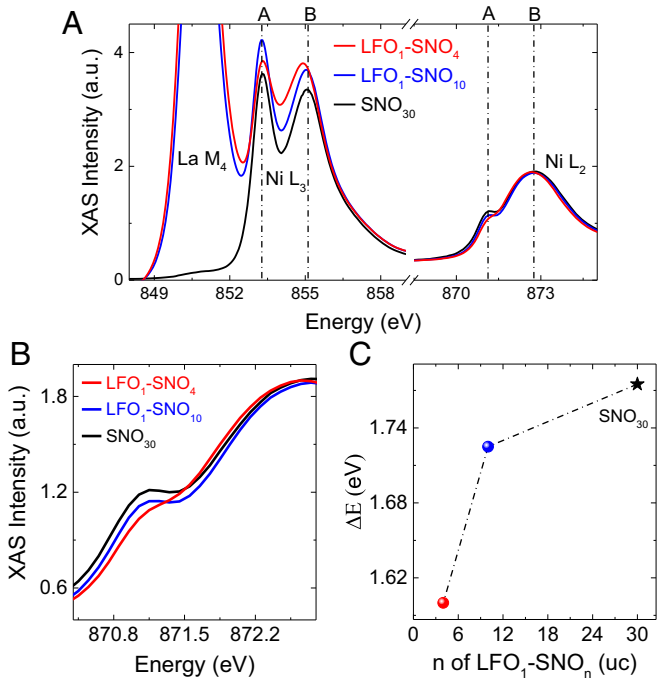

Fig. 3. Electronic structure of nickelate SLs. (*A*) XAS of Ni $L_{2,3}$ edge. (*B*) Zoomed-in spectra of Ni L_2 edge. (*C*) Peak splitting energy $\Delta E = E_B - E_A$ of LFO_1–SNO_n SLs and SNO_{30} film. The XAS was measured at 22 K.

discussed above in Fig. 1. Within the SL region, a trapezoidal wave-like Φ_N-profile is observed with a minimum angle exhibited by the LFO single layer and a plateau in the central part of each SNO layer. Closer to the LFO layer, the Φ_N of SNO becomes smaller. Upon reducing the SNO to 4 uc, the whole SNO layer is now under the impact of interfacial structure constraint, and thus, the Φ_N-profile is changed into a more triangular wave-like shape.

The profiles of octahedral tilt angle β_N (= β/β_{NGO}) around the [001] axis (see definition in Fig. 2*B*) are estimated from ABF images (*SI Appendix*, section 5). This tilt angle β corresponds in fact to the projection of α_T on (001) planes. Similar to the antipolar distortion Φ_N, the β_N becomes smaller near the LFO/SNO interface, and a periodic modulation of β_N is observed across the SL as shown in Fig. 2*E*. The modulation of the β_N of SNO layer is weakened when the SNO thickness is increased from 4 to 10 uc. The stretching or bending of the Ni–O bond should also change the lattice constant. This scenario is confirmed from the profile of out-of-plane lattice constant (*c*). As shown in Fig. 2*F*, the lattice parameter *c* of LFO within the SL region is smaller than that in the 4-uc LFO buffer region. Near the LFO/SNO interface, the *c* of the SNO becomes larger than that in the central region of the SNO layer. The larger (smaller) *c* of LFO or SNO corresponds to smaller (larger) tilt in LFO or SNO (Fig. 2 *D*–*F*). The mean values $<\Phi_N>$ ($<\beta_N>$) of SNO in LFO_1–SNO_{10} and LFO_1–SNO_4 SLs are 1.178 (0.976) and 1.049 (0.852), respectively. The reduced tilts and antipolar distortion demonstrate the effective control of octahedral distortion of SNO by intercalating the single LFO layer.

The electronic structures of SNO have been investigated by X-ray absorption spectroscopy (XAS). As shown in Fig. 3*A*, both Ni L_2 and L_3 edges are split into two (A and B) peaks as occurring in bulk $RNiO_3$ (26). The peak splitting energy ΔE ($\equiv E_B - E_A$) in LFO_1–SNO_4 is smaller than in LFO_1–SNO_{10}, while in LFO_1–SNO_{10} is similar to that in SNO_{30}. As shown by the zoomed-in view of the Ni L_2 edge in Fig. 3*B*, the two split peaks gradually merge with decreasing SNO thickness in LFO_1–SNO_n. The ΔE for the Ni L_3 edge is shown in Fig. 3*C*, clearly illustrating a smaller splitting energy due to the structure modulation by LFO. The splitting of the Ni L edge is suggested to depend on both the magnitude of the breathing mode distortion and the size of the Ni–O–Ni hopping interaction (27). A smaller splitting energy indicates a smaller Ni–O–Ni interaction and a smaller breathing distortion [$\delta d = (d_L - d_S)/2$], where d_L and d_S are the long and short Ni–O bonds, respectively (27). The XAS of the Ni $L_{2,3}$ edge shown in Fig. 3*A* also suggests the absence of Ni^{2+} and no change of the valence of Ni, excluding possible charge transfer between LFO and SNO layers.

Concomitant to lattice and electronic structure modulations, a significant change of transport properties in LFO_1–SNO_n SLs has been achieved. As shown in Fig. 4*A*, a giant enhancement of conductivity is observed in LFO_1–SNO_4 SL. The characteristic MIT temperature T_{MIT} is reflected from the resistivity inflection point $\left(\frac{d\ln\rho}{d1/T}|_{max}\right)$ (28) as shown in Fig. 4*A*, *Inset*. The T_{MIT} of LFO_1–SNO_4 is 78 K, much lower than that of SNO_{30} film (356 K). With increasing SNO thickness, the T_{MIT} moves toward that of bulk SNO films, coincident with the smaller structural modulation by LFO as the SNO thickness increases. The thickness (n) of SNO within LFO_1–SNO_n behaves similarly to the tolerance factor, monotonically controlling the transition temperatures (*SI Appendix*, section 6).

The decay nature of the geometric constraint imposed by the octahedral network across the interface allows us to rationally design the octahedral tilt distortion via either changing the thickness of the SNO layer or a delicate choice of the tilt-control layer. As an illustration of the designed functionality by engineering the nature of TCL, a $LaCrO_3$ (LCO) layer was used to fabricate a LCO_1–SNO_4 SL and compare with the LFO_1–SNO_4 SL. LCO shares the same orthorhombic structure and similar octahedral tilt with LFO but has a smaller lattice mismatch of 0.6% with NGO than LFO/NGO of 1.8%. LCO is expected to exhibit more bending of the Cr–O–Cr bond and, therefore, have less impact on the tilt of the SNO (22, 23). The effect of LCO on the SNO structural modulation was investigated as well by STEM, as shown in Fig. 4*B*. Near the LCO/SNO interface, both the Φ_N and β_N of SNO are found to be reduced as occurring in

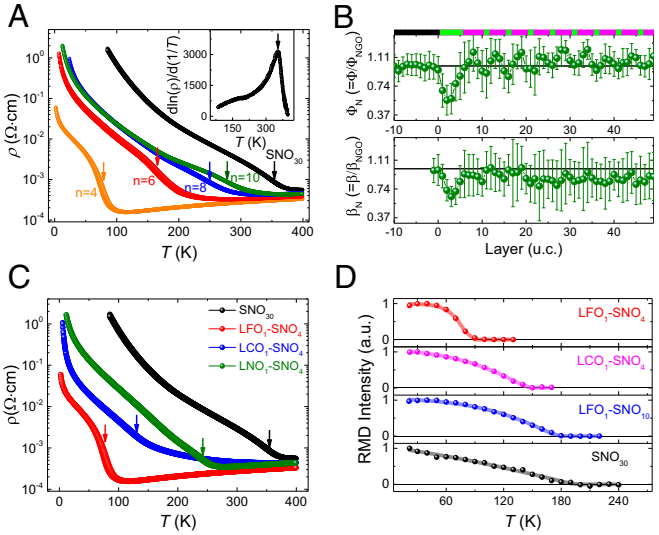

Fig. 4. Transport and magnetic properties of tilt engineered nickelate SLs. (*A*) Temperature-dependent resistivity of LFO_1–SNO_n SLs (n = 4–10) and 30 uc SNO film (SNO_{30}). *Inset* shows the first derivative $\frac{d\ln\rho}{d1/T}$ of the SNO_{30} sample. The arrows in *A* and *C* indicate the resistive inflection points derived from $d\frac{d\ln\rho}{d1/T}|_{max}$. (*B*) Layer-dependent profiles of antipolar motions (Φ) and octahedral tilt angle (β) of LCO_1–SNO_4 SL. The chemical profile is schematically shown on *Top*: black (NGO), green (LCO), and purple (SNO). (*D*) Temperature-dependent intensity of (1/4,1/4,1/4) magnetic Bragg reflection peak.

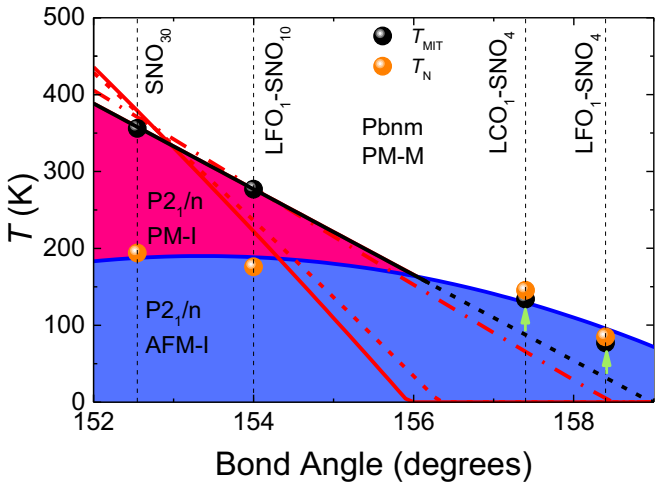

Fig. 5. Temperature phase diagram of nickelate SLs as a function of the mean Ni–O–Ni bond angle. The mean bond angle is converted from mean tilt angle α_T (see *Materials and Methods*). The black dots (T_{MIT}) and orange dots (T_N) are experimental data. The theoretical evolution of T_{MIT} has been estimated while constraining the tilt angle α_T as imposed by the TCL and (*i*) relaxing self-consistently the rotation angle α_R ($\Delta\alpha_R \sim -1.5\%$, full red line), (*ii*) constraining the rotation angle to keep it fixed ($\Delta\alpha_R = 0\%$, dashed red line), or (*iii*) constraining further the rotation angle to increase it slightly ($\Delta\alpha_R \sim +3\%$, dash-dot red line). See *Materials and Methods* for the explanation of the parameter $\Delta\alpha_R$.

LFO_1–SNO_4. However, the $<\Phi_N>$ and $<\beta_N>$ of SNO within LCO_1–SNO_4 SL are 1.079 and 0.890, respectively, bigger than the values for LFO_1–SNO_4, as mentioned above. Accordingly, the LCO_1–SNO_4 SL shows higher conductivity than non-engineered SNO_{30} but is less conductive than the LFO_1–SNO_4 SL (Fig. 4*C*). The significant impact from LFO is further illustrated by comparing to the $(LaNiO_3)_1$–SNO_4 (LNO_1–SNO_4) SL. As shown in Fig. 4*C*, LNO_1–SNO_4 exhibits a much higher T_{MIT} (=240 K) than LFO_1–SNO_4. Although LNO has a little smaller tilt in bulk (5.3°) than that of bulk LFO (6.8°), the LNO layer is under tensile strain, which increases the tilt, in contrast to the highly compressive strain imposed on the LFO layer. The higher conductivity in LFO_1–SNO_4 than LNO_1–SNO_4 further reveals a pivotal role of the structural effect rather than any possible chemical reconstruction at the interface.

In addition, the Néel temperature (T_N) was measured using resonant magnetic diffraction (RMD) (27, 29). The RMD signal was taken at the Ni L_3 resonance. Fig. 4*D* displays the temperature-dependent intensity of the (1/4,1/4,1/4) magnetic Bragg reflection peak, which arises from the E′-type antiferromagnetic (E′-AFM) ordering of the nickelates. The Néel temperature is found to vary significantly when introducing interfacial structure modulation. The T_N of the SNO_{30} film is ~194 K, while it is ~85 K for the LFO_1–SNO_4. For LFO_1–SNO_{10}, the effect of the LFO layer becomes weaker and the T_N is around 176 K, close to the SNO_{30} film. The T_N of LCO_1–SNO_4 is ~146 K, in between LFO_1–SNO_4 and LFO_1–SNO_{10}.

With the obtained T_N and T_{MIT}, a phase diagram is constructed using the mean Ni–O–Ni bond angle as a control parameter (Fig. 5). Here, the mean Ni–O–Ni bond angles are converted from mean values of β_N (see *Materials and Methods*). It is found that the T_{MIT} monotonically changes with the bond angle. For films with relatively small Ni–O–Ni bond angles and large T_{MIT} (>~200 K), T_N and T_{MIT} are decoupled and T_{MIT} decreases relatively abruptly as the bond angle increases. According to that trend, T_{MIT} should be below T_N at large bond angles; in that region, however, the T_{MIT} is further promoted by the appearance of the E′-type AFM order and T_{MIT} becomes pinned at T_N, in line with the discussion in ref. 19 and in agreement with bulk phase diagram (10). Therefore, the geometric design of the octahedral network produces a bulk-like phase diagram of the whole nickelate family but using only one compound SNO (Fig. 5 and *SI Appendix*, section 6). Our results also highlight the effect of local octahedral distortion at the atomic scale on the nickelate electronic states, confirming the central role the NiO_6 octahedral tilt in determining the properties of nickelates.

The explicit link between the controlled amplitude of the Ni–O–Ni bond angle and the observed evolution of T_{MIT} can be further supported theoretically using the Landau-type model of ref. 19, assigning the MIT to a triggered phase transition arising from the softening of the breathing distortion by oxygen tilts and rotation and with parameters directly derived from first principles. Starting from the set of parameters associated to the effective tolerance factor yielding a T_{MIT} equal to that of SNO_{30}, we can mimic the role of the TCL by forcing artificially the tilt mode amplitude (i.e., rescaling its energy curvature; see *Materials and Methods*) and investigating the subsequent impact on T_{MIT}. This can be done while allowing self-consistent relaxation of the rotation mode or by constraining it additionally so that it remains constant or is slightly amplified. The predictions of the model are summarized in Fig. 5 and compared with the experimentally obtained correlation between T_{MIT} and the bond angle. Note that here the model is restricted to structural degrees of freedom and neglects the emergence of a magnetic order at T_N. The agreement observed between theory and experiment confirms the central role of the oxygen tilts in tuning T_{MIT}. The model further suggests that rotations might be slightly amplified as the tilts are reduced.

This efficient tuning is exploited practically to move T_{MIT} close to room temperature and switch the resistance by an external stimulus. Here, we propose and use an approach to tune the resistance of nickelates through light illumination at specific wavelengths. Fig. 6*A*, *Inset* presents a sketch of the electronic structure of a nickelate in its insulating phase as usually understood today. The conduction band is formed by e_g* states (antibonding states between Ni 3d and O 2p states, of predominant oxygen character) whose density of

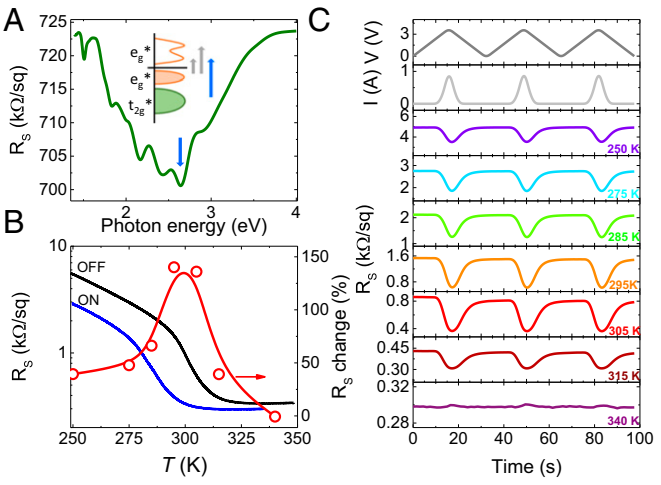

Fig. 6. Light-induced resistance switching in nickelate SLs. (*A*) Dependence of the sheet resistance with illuminating photon energy at 70 K for a NNO_1–SNO_2 SL. The sketch describes the different optical transitions in nickelates, and the down-pointing blue arrow shows the energy corresponding to the t_{2g}* → e_g* transition at ~2.7 eV. (*B*) Temperature dependence of the sheet resistance of NNO_1–SNO_2 SL (left axis) without (black) and with illumination (blue) with a blue LED ($h\nu$ = 2.69 eV) powered with 1 A. Relative resistance change (right axis) induced by illumination. The symbols (right axis) correspond to the data of *C*. (*C*, *Top* two) Voltage and current applied to the blue LED vs. time. (*C*, *Bottom* seven) Time dependence of the resistance upon illuminating the NNO_1–SNO_2 sample with the blue LED at different temperatures.

states shows a double peak shape with a local minimum (30). Below the Fermi level, the valence band has a similar character, in line with the negative-charge transfer nature of nickelates. Further down in energy lie the t_{2g}^* states, with dominant Ni 3d character. This electronic structure allows for three main optical transitions (Fig. 6*A*, *Inset*) (31). The deeper t_{2g}^* to e_g^* state transition (blue arrow) corresponds to transferring electrons from a 3d-like state to an O 2p-like state. Given that the occupancy of O 2p states is directly related to the level of covalence, a $t_{2g}^* \rightarrow e_g^*$ transition should intensify the covalent character and then enhance conductivity (15). More generally, photo transfer of electrons from large to small Ni cages will bring the system closer to the metallic electronic configuration of the Pbnm phase.

To realize room temperature oxide electronics for practical applications, several different TCLs have been explored to induce a first-order room temperature MIT, and $NdNiO_3$ (NNO) is found to be an ideal candidate (Fig. 4 and *SI Appendix*, section 7). A first-order MIT near room temperature was obtained in a $(NNO_1/SNO_2)_{10}$ (NNO_1–SNO_2) SL (*SI Appendix*, section 7). Fig. 6*A* shows its resistance at 70 K (well into the insulating state) upon low-power illumination at different photon energies. The resistance shows a minimum for an energy corresponding to the $t_{2g}^* \rightarrow e_g^*$ transition, which is consistent with the photo-doping mechanism described above. Fig. 6*B* presents the temperature dependence of the resistance of the sample with and without 2.69 eV high-power blue light, nonisothermal illumination. The MIT temperature shifts down by ∼20 K with the light on, yielding a maximum light-induced resistance change near 300 K. Fig. 6*C* shows the evolution of the resistance upon illumination with blue light pulses at different temperatures. Consistent with the data in Fig. 6*B*, the resistance switching effect is maximized at 300 K, amounting to nearly 150%. In *SI Appendix*, we show data for isothermal illumination and for a LFO_1–SNO_{10} SL. Since we were using long illumination pulses, sample heating due to light absorption was probably the main process at play, causing an apparent shift of the MIT temperature. However, the observed maximum optical switching near room temperature would strongly imply that the photo-doping mechanism proposed above should also yield a resistance switching effect for ultrafast (sub ps) pulses with a photon energy corresponding to the $t_{2g}^* \rightarrow e_g^*$ transition (see also *SI Appendix*, section 8). In any case, our data qualify engineered nickelates as room temperature photoresistors based on a correlated material.

Discussion and Conclusion

In conclusion, we demonstrated the remote control of ground state properties of nickelates through interfacial tilt pattern modulation using a TCL. By manipulating two independent adjustable parameters—the nature of the tilt-control material, and the relative thicknesses of the target and tilt-control materials—we obtained pseudocontinuous modulation of octahedral tilt and fine-tuning of the materials' properties. Our results visualized the monotonic change of the MIT with varying octahedral tilt, remarkably underlining the role of the Ni–O–Ni bond angle in determining the electronic ground state of the nickelates and supporting the structurally triggered mechanism proposed in ref. 19. By finely tuning the oxygen network, we are already able to achieve a near-room temperature MIT and a giant room temperature optical switching of resistance. The interfacial tilt pattern modulation using a TCL can be viewed as a structural analog of modulation doping in semiconductors, which has been a breakthrough discovery and led to both the observation of the fractional quantum Hall effect and to faster microelectronic circuits. This interface modulation tilt control can be applied directly to other perovksite materials, opening up new perspectives for the rational design of new classes of quantum materials for next-generation electronics applications.

Materials and Methods

The SNO, LNO, LFO, and LCO films or layers were deposited on atomic flat NGO substrates at a laser fluence of 2 J/cm^2 by PLD technique. The XRD was performed by PANalytical-X'Pert materials research diffractometer (MRD) at high-resolution mode. Transport properties were measured by using a Quantum Design Physical Properties Measurement System (PPMS) in a van-der-Pauw geometry.

STEM was performed on the Qu-Ant-EM instrument at the University of Antwerp. Cross-sectional cuts of the samples along the [1-10] and [001] directions were prepared using a FEI Helios 650 dual-beam Focused Ion Beam device. Satisfactory samples were prepared using low-energy ion beam final thinning subsequent to a protection of the sample surface by sputtering of a 30 nm-thick carbon protection layer, followed by E-beam deposition of Platinum as a first step to the FIB lamella preparation procedure. For imaging and EELS, the microscope was operated in STEM at 300 kV acceleration voltage with a convergence semiangle of 21 mrad, providing a probe size of ∼0.8 Å. The collection semiangle are 8 to 17 mrad and 44–190 mrad for ABF and high-angle annular dark field (HAADF) imaging, respectively. The collection angle for EELS was 69 mrad. Image processing and analysis is detailed in *SI Appendix*. Simulations of ABF-STEM images of SNO along $[001]_{or}$ and $[1\text{-}10]_{or}$ zone axes were made with QSTEM at conditions of probe size 0.7 Å, 300 kV, de focus −1.7 nm, C3 = 1 μm, convergence angle 21 mrad, 15 configurations for TDS, collection angle 8–17 mrad, and 15 nm thickness.

The XAS and RMD were performed using an in-vacuum four-circle diffractometer at the Resonant Elastic and Inelastic X-Ray Scattering (REIXS) beamline at Canadian Light Source (CLS) in Saskatoon, Canada. The beamline has a flux of 5×10^{12} photons per second and photon energy resolution of 10^{-4} eV. The base pressure of the diffractometer chamber was kept lower than 10^{-9} Torr. The XAS spectra were measured using the total electron yield method, with the incident photons at an angle of 30° from the surface. At the Ni $L_{2,3}$ edge, measurements with π and σ polarizations were averaged.

The Landau-type modeling was performed relying on the expression provided in ref. 19 and related set of parameters directly fitted from first-principles DFT calculations (see supplementary material in ref. 19). The effective tolerance factor was selected to get a MIT corresponding to that experimentally observed in the SNO_{30} sample (T_{MIT} = 356 K). Then, to mimic the role of the TCL on the tilt mode, the energy curvature of the latter was renormalized by adding a prefactor $(1 - x)$ in front of the tilt quadratic coefficient. Tuning x, we can get the evolution of the tilt amplitude at room temperature (α_T directly linked to the Ni–O–Ni bond angle) and of the corresponding T_{MIT} in terms of the external constraint imposed on the tilt mode. Results are reported in Fig. 5, in which we plot the evolution of T_{MIT} with respect to that of the Ni–O–Ni bond angle at room temperature for direct comparison with experimental data. Since tilt and rotation modes are coupled within the Landau model through a biquadratic term, tuning the tilt amplitude also indirectly affects the rotation angle. Since we have no direct information on the effects of the TCL and epitaxial strain on the latter, calculations were performed (*i*) relaxing self-consistently the rotation angle α_R, which progressively evolves with α_T (for the largest constraint imposed on α_T in Fig. 5, the deviation of α_R at T_{MIT} with respect to its natural amplitude—i.e., value in bulk without constraint—is $\Delta\alpha_R \sim -1.5\%$); (*ii*) constraining the rotation angle to force it to remain unaffected ($\Delta\alpha_R = 0\%$); and (*iii*) constraining the rotation angle to increase it slightly (here the coupling between rotations and tilts has been slightly modified so that for the largest constraint imposed on α_T in Fig. 5, $\Delta\alpha_R \sim +3\%$). The tilt angle amplitude α_T, as accessible from the Landau model, and its projection on (001) planes, as measured experimentally, are both related to the Ni–O–Ni bond angle reported in Fig. 5 through $\theta = 180 - 2\,\alpha_T = 2\,\sin^{-1}[1/(1 + 2\,\tan^2\beta)^{1/2}]$.

Transport measurements under illumination were performed in a cryostation provided by Montana Instrument with uncoated windows presenting 90% transmittance in the visible range. Two different configurations were used for characterizing the thermal response of the samples. In setup 1, the layer was thermally connected to the cold finger of the cryostat. To do so, we added thermal grease to the edges of the sample in such a way that the NGO substrate was thermally connected to the sample holder. In setup 2, an insulating layer was added between the sample and the sample holder such that there was no thermal contact between the layer and the cold finger of the cryostat. The sheet resistance was determined by biasing with a current of 10 μA.

ACKNOWLEDGMENTS. We acknowledge Prof. Z. Zhong for stimulated discussion. M.H., G.K., and G.R. acknowledge funding from the 2-Dimensional Electron Systems in Complex Oxides (DESCO) program of the Dutch Foundation for Fundamental Research on Matter (FOM) with financial support from the Netherlands Organization for Scientific Research (NWO). This work was funded by the European Union Council under the 7th Framework

Program (FP7) Grant NMP3-LA-2010-246102 IFOX. J.V., S.V.A., N.G., and K.M.-C. acknowledge funding from FWO Projects G.0044.13N, G.0374.13N, G. 0368.15N, and G.0369.15N. The Qu-Ant-EM microscope was partly funded by the Hercules fund from the Flemish Government. N.G. acknowledges funding from the European Research Council (ERC) under the FP7, ERC Starting Grant 278510 VORTEX. N.G. and J.V. acknowledge financial support from the European Union under an FP7 contract for an Integrated Infrastructure Initiative (Reference No. 312483-ESTEEM2). The Canadian work was supported by Natural Sciences and Engineering Research Council of Canada (NSERC) and the Max Planck-University of British Columbia (UBC) Centre for Quantum Materials. Some experiments for this work were performed at the Canadian Light Source, which is funded by the Canada Foundation for Innovation, NSERC, the National Research Council of Canada, the Canadian Institutes of Health Research, the Government of Saskatchewan, Western Economic Diversification Canada, and the University of Saskatchewan. M.B. acknowledges funding from the ERC under FP7, ERC Consolidator Grant MINT 615759. A.M. and P.G. were supported by the Action de Recherche Concertée (ARC) project AIMED and National Scientific Research Funds (F.R.S.-FNRS) Research Project HiT4FiT and acknowledge access to Céci computing facilities funded by F.R.S.-FNRS (Grant 2.5020.1), Tier-1 supercomputer of the Fédération Wallonie-Bruxelles funded by the Walloon Region (Grant 1117545), and high-performance computing resources from the Partnership for Advanced Computing in Europe (PLACE) project Megapasta.

1. Hwang HY, et al. (2012) Emergent phenomena at oxide interfaces. *Nat Mater* 11: 103–113.
2. Choi KJ, et al. (2004) Enhancement of ferroelectricity in strained $BaTiO_3$ thin films. *Science* 306:1005–1009.
3. Logvenov G, Gozar A, Bozovic I (2009) High-temperature superconductivity in a single copper-oxygen plane. *Science* 326:699–702.
4. Boris AV, et al. (2011) Dimensionality control of electronic phase transitions in nickel-oxide superlattices. *Science* 332:937–940.
5. Yadav AK, et al. (2016) Observation of polar vortices in oxide superlattices. *Nature* 530:198–201, and erratum (2016) 534:138.
6. Chakhalian J, et al. (2007) Orbital reconstruction and covalent bonding at an oxide interface. *Science* 318:1114–1117.
7. Kim TH, et al. (2016) Polar metals by geometric design. *Nature* 533:68–72.
8. Pavarini E, et al. (2004) Mott transition and suppression of orbital fluctuations in orthorhombic $3d^1$ perovskites. *Phys Rev Lett* 92:176403.
9. Zhou JS, Goodenough JB (2003) Orbital order-disorder transition in single-valent manganites. *Phys Rev B Condens Matter Mater Phys* 68:144406.
10. Medarde ML (1997) Structural, magnetic and electronic properties of $RNiO_3$ perovskites (R = rare earth). *J Phys Condens Matter* 9:1679–1707.
11. King PDC, et al. (2014) Atomic-scale control of competing electronic phases in ultrathin $LaNiO_3$. *Nat Nanotechnol* 9:443–447.
12. Chaloupka J, Khaliullin G (2008) Orbital order and possible superconductivity in $LaNiO_3/LaMO_3$ superlattices. *Phys Rev Lett* 100:016404.
13. Bisogni V, et al. (2016) Ground-state oxygen holes and the metal-insulator transition in the negative charge-transfer rare-earth nickelates. *Nat Commun* 7:13017.
14. Scherwitzl R, et al. (2011) Metal-insulator transition in ultrathin $LaNiO_3$ films. *Phys Rev Lett* 106:246403.
15. Grisolia MN, et al. (2016) Hybridization-controlled charge transfer and induced magnetism at correlated oxide interfaces. *Nat Phys* 12:484–492.
16. Zhou J-S, Goodenough JB, Dabrowski B (2005) Exchange interaction in the insulating phase of $RNiO_3$. *Phys Rev Lett* 95:127204.
17. Shi J, Zhou Y, Ramanathan S (2014) Colossal resistance switching and band gap modulation in a perovskite nickelate by electron doping. *Nat Commun* 5:4860.
18. Shi J, Ha SD, Zhou Y, Schoofs F, Ramanathan S (2013) A correlated nickelate synaptic transistor. *Nat Commun* 4:2676.
19. Mercy A, Bieder J, Íñiguez J, Ghosez P (2017) Structurally triggered metal-insulator transition in rare-earth nickelates. *Nat Commun* 8:1677.
20. Rondinelli JM, May SJ, Freeland JW (2012) Control of octahedral connectivity in perovskite oxide heterostructures: An emerging route to multifunctional materials discovery. *MRS Bull* 37:261–270.
21. Liao Z, et al. (2016) Controlled lateral anisotropy in correlated manganite heterostructures by interface-engineered oxygen octahedral coupling. *Nat Mater* 15: 425–431.
22. May SJ, et al. (2010) Quantifying octahedral rotations in strained perovskite oxide films. *Phys Rev B Condens Matter Mater Phys* 82:014110.
23. Vailionis A, et al. (2011) Misfit strain accommodation in epitaxial ABO_3 perovskites: Lattice rotations and lattice modulations. *Phys Rev B Condens Matter Mater Phys* 83: 064101.
24. Amisi S, Bousquet E, Katcho K, Ghosez P (2012) First-principles study of structural and vibrational properties of $SrZrO_3$. *Phys Rev B Condens Matter Mater Phys* 85:064112.
25. Miao N, Bristowe NC, Xu B, Verstraete MJ, Ghosez P (2014) First-principles study of the lattice dynamical properties of strontium ruthenate. *J Phys Condens Matter* 26: 035401.
26. Freeland JW, van Veenendaal M, Chakhalian J (2016) Evolution of electronic structure across the rare-earth $RNiO_3$ series. *J Electron Spectrosc Relat Phenom* 208:56–62.
27. Green RJ, Haverkort MW, Sawatzky GA (2016) Bond disproportionation and dynamical charge fluctuations in the perovskite rare-earth nickelates. *Phys Rev B* 94: 195127.
28. Liu J, et al. (2013) Heterointerface engineered electronic and magnetic phases of $NdNiO_3$ thin films. *Nat Commun* 4:2714.
29. Hawthorn DG, et al. (2011) An in-vacuum diffractometer for resonant elastic soft X-ray scattering. *Rev Sci Instrum* 82:073104.
30. Ruppen J, et al. (2015) Optical spectroscopy and the nature of the insulating state of rare-earth nickelate. *Phys Rev B Condens Matter Mater Phys* 92:155145, and erratum (2017) 95:239903.
31. Stewart MK, Liu J, Kareev M, Chakhalian J, Basov DN (2011) Mott physics near the insulator-to-metal transition in $NdNiO_3$. *Phys Rev Lett* 107:176401.